Surface Analysis of Pristine and Cycled NMC/Graphite Lithium-Ion Battery Electrodes: Addressing the Measurement Challenges

Sofia Marchesini[1], Benjamen P. Reed[1], Helen Jones[1], Lidija Matjacic[1a], Timothy E. Rosser[1b], Yundong Zhou[1], Barry Brennan[1c], Mariavitalia Tiddia[1d], Rhodri Jervis[2,3], Melanie. J. Loveridge[3,4], Rinaldo Raccichini[1], Juyeon Park[1], Andrew J. Wain[1], Gareth Hinds[1], Ian S. Gilmore[1], Alexander G. Shard[1], Andrew J. Pollard[1]*

[1] National Physical Laboratory, Hampton Road, Teddington TW11 0LW, United Kingdom

[2] Electrochemical Innovation Lab, Department of Chemical Engineering, University College of London, London SW7 2AZ, United Kingdom

[3] The Faraday Institution, Quad One, Harwell Science and Innovation Campus, Didcot OX11 0RA, United Kingdom

[4] Electrochemical Materials Group, Warwick Manufacturing Group, University of Warwick, Coventry CV4 7AL, United Kingdom

ABSTRACT

Lithium-ion batteries are the most ubiquitous energy storage devices in our everyday lives. However, their energy storage capacity fades over time due to chemical and structural changes in their components, *via* different degradation mechanisms. Understanding and mitigating

these degradation mechanisms is key to reducing capacity fade, thereby enabling improvement in the performance and lifetime of Li-ion batteries, supporting the energy transition to renewables and electrification. In this endeavour, surface analysis techniques are commonly employed to characterise the chemistry and structure at reactive interfaces, where most changes are observed as batteries age. However, battery electrodes are complex systems containing unstable compounds, with large heterogeneities in material properties. Moreover, different degradation mechanisms can affect multiple material properties and occur simultaneously, meaning that a range of complementary techniques must be utilised to obtain a complete picture of electrode degradation. The combination of these issues and the lack of standard measurement protocols and guidelines for data interpretation can lead to a lack of trust in data. Herein, we discuss measurement challenges that affect several key surface analysis techniques being used for Li-ion battery degradation studies: focused ion beam scanning electron microscopy, X-ray photoelectron spectroscopy, Raman spectroscopy, and time-of-flight secondary ion mass spectrometry. We provide recommendations for each technique to improve reproducibility and reduce uncertainty in the analysis of NMC/graphite Li-ion battery electrodes. We also highlight some key measurement issues that should be addressed in future investigations.

KEYWORDS: Li-ion batteries, surface analysis, solid electrolyte interphase, XPS, Raman spectroscopy, ToF-SIMS, FIB-SEM.

1. INTRODUCTION

The research and development of next-generation energy storage devices is a high priority for governments worldwide.[1] Such devices are required if we are to harness the full potential of renewable energy sources to reduce our reliance on fossil fuels and meet global and national net-zero greenhouse gas emission targets. Lithium-ion batteries (LIBs) are among the most

widely used energy storage systems, particularly in high energy density applications, with graphite negative electrodes (NE) and lithium transition metal oxide positive electrodes (PE) still used as the most common LIB active materials. This is due to their high energy density, reversible de/lithiation ability, and relatively low cost, making them particularly suitable for use in portable electronics and the automotive industry.[2] Amongst PE materials, lithium nickel manganese cobalt oxides (NMCs, $LiNi_xMn_yCo_zO_2$), particularly nickel rich NMCs (e.g. NMC 811: $x = 0.8$; $y = 0.1$; $z = 0.1$), display some of the highest specific capacities.[2]

However, since their application has diversified into many larger devices beyond small, portable electronics, performance targets for LIBs have increased significantly. As such, there are features of LIBs that still require improvement if they are to continue to support the electrification transition of many sectors, such as transport, heating, and grid storage. Some of the technical gaps identified in LIB technology for the automotive industry are energy and power density, safety, durability, and recyclability.[2] In LIBs these gaps are directly related to degradation mechanisms leading to a decrease in battery performance with time and use.[2,3]

Degradation mechanisms are a collection of complex and interdependent physical and chemical processes occurring, often simultaneously, in different battery components. In the "Degradation Mechanisms in LIB Electrodes" section in the Supporting Information (SI) we summarise key degradation mechanisms in typical LIB electrodes (namely NMC PE and graphite NE) as described in more in-depth reviews.[3,4] This section is important to understand the nature, scale, and location of critical materials properties that change with degradation. The analysis of these physicochemical changes requires accurate and reproducible measurement methods to understand degradation processes and ultimately mitigate them. Within these, of particular importance is the measurement of properties of surfaces and interfaces, where most reactions occur during battery operation. On the surface of the NMC PE some of the main

degradation mechanisms are: formation of nickel rock salt phase, deposition of electrolyte decomposition products (cathode electrolyte interphase, CEI), microscale cracks, dissolution of transition metals (TM), and deposition of chemical species generated by parasitic reactions. At graphite NE surfaces the following degradation mechanisms can occur: deposition of electrolyte decomposition products (solid electrolyte interphase (SEI)), lithium plating, deposition of TM from the PE, and cracks.[3,4]

At the same time, degradation processes result in measurable changes at different length-scales (from nano- to macroscale) and from the surface to bulk. Therefore, a rational selection of complementary techniques must be used to provide a full picture of degradation mechanisms. Measurement protocols must be standardised to enable reliable comparison of data, thereby achieving a valid framework to underpin improvements in both battery performance and lifetime. Herein, we discuss measurement techniques that are often used to investigate these material properties and provide a metrological perspective on the related structural and chemical measurement challenges associated with LIBs. Illustrative examples of measurement challenges and solutions are provided using a range of material characterisation techniques, such as focused ion beam scanning electron microscopy (FIB-SEM), Raman spectroscopy, X-ray photoelectron spectroscopy (XPS) and time of flight secondary ion mass spectrometry (ToF-SIMS), both before and after electrochemical cycling. To provide more meaningful conclusions these complementary techniques have been applied to the same set of samples.

2. EXPERIMENTAL SECTION

2.1.Materials

In this study, eight electrodes (four NMC 811 PE and four graphite NE) were harvested from four pouch cells at different stages of ageing (see Table S1). Each harvested electrode consisted of a 1 cm × 1 cm strip cut from the parent electrode of the cell, which was further divided into

smaller samples for each technique (see 'Methods'). The full details for these samples (e.g. composition, electrolyte and cycling conditions) and their preparation for *ex situ* analysis (transfer between glovebox and instrument) are provided in the "Materials" section in the SI. Electrodes that had not been exposed to electrolyte ("pristine") and electrodes that had been charged to 3.8 V after electrolyte injection but not electrochemically cycled ("uncycled") were analysed for reference. Pairs of electrodes that had been cycled with upper voltage limits of 4.2 V and 4.3 V, respectively, were also analysed at their end of life (EoL), corresponding to a decrease to 80 % of their initial capacity. The cell cycled with an upper voltage limit of 4.3 V reached its EoL after a shorter number of cycles (~400) compared to the cell cycled with an upper voltage limit of 4.2 V (~700 cycles).

2.2.Methods

Full details of sample analysis (e.g. measurement parameters, data analysis and software processing, peak fitting) can be found in the "Methods" section of the SI.

2.2.1. SEM and FIB-SEM

Samples were prepared in an Ar-filled glovebox and quickly (< 5 min) transferred to the FIB-SEM instrument (Zeiss Auriga 60, Germany) to minimise exposure to air. The images were taken with an Everhart-Thornley secondary electron detector with an acceleration voltage of 3 kV and an aperture size of 30 µm, at a working distance of 5 mm. For the FIB cross-sectioning, the stage was tilted to 54° so it was perpendicular to the focused ion beam, where beam currents of down to 30 kV: 1 nA were used for milling.

2.2.2. Raman spectroscopy

Samples were mounted inside the Ar-filled glovebox into an airtight cell equipped with a sapphire window, which allowed for samples to be analysed under a protective argon

atmosphere. Measurements were performed using a Raman spectrometer (inVia Qontor, Renishaw, UK). Raman mapping was performed using a 532 nm laser with < 1.32 mW (PE) and < 2.50 mW (NE) power incident at the surface, with a 50× objective lens of 0.5 NA and a 2400 l/mm grating.

2.2.3. XPS

Samples were transferred from the Ar-filled glovebox to the XPS chamber using an inert atmosphere sample transporter (herein, transporter) provided by Kratos Analytical Ltd (UK). XPS analysis was conducted using a Kratos Analytical Ltd AXIS Ultra DLD operating in 'hybrid' lens mode, and equipped with a monochromatic Al Kα X-ray source (15 kV, 5 mA).

2.2.4. ToF-SIMS

The samples were mounted on a sample holder inside the Ar-filled glovebox and transferred under Ar atmosphere in a zip lock bag to the instrument. The samples were briefly (< 5 min) exposed to atmosphere during transfer to the ToF-SIMS instrument until vacuum conditions were established.

ToF-SIMS was performed using an IONTOF GmbH (Germany) ToF.SIMS V instrument, comprising of a 30 keV Bi_3 primary-ion gun for analysis and an Ar gas cluster ion gun for depth profiling, and an IONTOF GmbH ToF.SIMS IV instrument with a 25 keV Bi_3 primary-ion gun for analysis and an Cs liquid metal ion gun for depth profiling.

3. RESULTS AND DISCUSSION

3.1.Scanning Electron Microscopy (SEM) and Focused Ion Beam SEM (FIB-SEM)

SEM combined with FIB milling is generally used to image both the surface and internal morphological features of electrode materials. FIB-SEM enables analysis of particle size, crack

formation, particle inter-connectivity, SEI thickness and morphology, macro-scale porosity, and lithium plating.[5–8]

Of particular importance is the analysis of the morphology of the SEI layer. One approach to improve surface morphological contrast with the electron beam is to image using a low electron acceleration voltage (~1 kV).[7] SEI thickness can vary from a few to hundreds of nanometres and is generally much thicker on the NE compared to the CEI on the PE. Therefore, while an SEI layer can be observed from SEM images of NE surfaces, it is not usually possible to distinguish the CEI layer on PE surfaces.[8] Examples of SEM images with and without FIB milling are shown in Figure 1a-c and Figure S2a,b,d,e,g-i (NE) and Figure 1d-f and Figure S2c,f,j-l (PE), revealing the morphology of these electrodes and the SEI on the NE. As shown in Figure 1c, an SEI layer can also form in internal graphite cracks and in between particles, known as "internal SEI", which could only be visualised using FIB milling to make precise cross-sections for imaging with SEM.

FIB-SEM can also aid in exposing sub-surface features such as microscale cracks that can allow the electrolyte to penetrate inside the NMC PE particles, leading to potential NiO rocksalt formation at interfaces. These cracks have often been associated with major capacity loss and an increase in impedance (examples of such cracks are observed in Figure 1f).[6] Microscale cracks can also cause particles to lose connectivity and therefore electrical conductivity. [6] In graphite NEs, it has been shown that cracks tend to originate at grain boundaries and in a direction parallel to the current collector as a result of volume changes.[9] When performing FIB milling on such uneven and porous samples, imaging artefacts are unavoidable, predominantly "curtaining", which is caused by different milling rates of different parts of the material; this is observed on the cross-sectional surface as vertical striping (see Figure 1f as an example).[10] It must be noted that decreasing beam currents were used during FIB-milling to clean the cross-

sectional surface (see Methods). Coating of the material with a protective layer (e.g. gold) before milling could also potentially be used to reduce beam damage.[11]

Previous studies have attempted to use SEM imaging to visualise areas with poor electrical conductivity by using lower electron beam accelerating voltages to detect charging effects and thereby infer the electrode percolation (i.e. areas with low conductivity appear brighter than expected in the SEM image).[12] For example, in NE samples (Figure 1b for cycled and Figure S2h for uncycled), the graphite particles are shown to charge preferentially near the SEI layer, likely due to its insulating properties. Image contrast is however also affected by topography, loose particles on the surface and sample composition. Therefore, the image data must be carefully interpreted when studying conductivity. Another issue to consider is beam-induced damage, which has been reported when high acceleration voltages are used, though this is more common in transmission electron microscopy (TEM).[13] Such damage can be minimised by reducing the acceleration voltage, using faster scanning speeds, or reducing the sample temperature.[14] Implanted gallium in the cross-sectional surface arising from FIB milling can also improve surface conductivity for the purpose of SEM imaging.

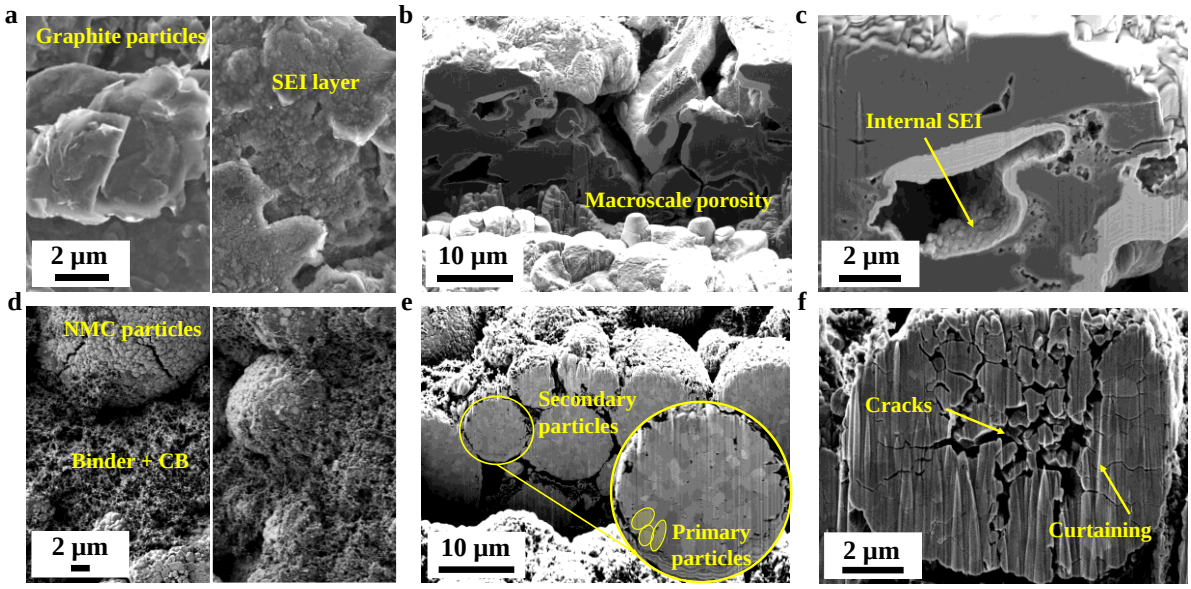

Figure 1. SEM and FIB-SEM images of a-c) graphite NE and d-f) NMC 811 PE before and after cycling. a) shows a pristine NE surface on the left and EoL 4.3 V NE on the right,

with a layer of SEI on the EoL 4.3 V NE surface; b) shows an EoL 4.3 V NE cross-section revealing internal macro-scale porosity and particle size; c) shows an internal SEI formed in a pore in an EoL 4.3 V NE; d) shows pristine and EoL 4.3 V PE surfaces; e) shows a cross-section of a pristine PE with secondary and primary NMC particles; f) shows cracks and loss of connectivity between primary NMC particles as well as some curtaining effects in the EoL 4.3 V PE.

High spatial resolution can be achieved in SEM images, yet only a relatively very small area is investigated within a single image compared to the size of the sample itself. Therefore, care must be taken to image a representative portion of the sample, for instance by sampling multiple images of different areas of the same electrode or comparable electrodes, so that definitive conclusions of the abundance of certain features can be made in a quantitative manner. This can be achieved using collages of images for different areas with the total number of images dependent on the imaged area and features observed.

Quantitative information for a localised area can also be extracted from 3D reconstructions using a FIB to remove slices of material and collecting consecutive SEM images.[15] Some of the information extracted from these reconstructions includes the areal fraction of microscale cracks,[16] particle radii, volume fraction of active material, particle size,[17] porosity,[5] and surface-to-volume ratio of different components.[15] 3D reconstructions can be fed into mathematical models to provide a representation of battery electrodes in electrochemical simulations.[15] When performing 3D reconstructions from FIB-SEM serial sectioning images (FIB-SEM tomography), users must be wary of potential image distortion artefacts, caused by sample charging and drifting effects.[10] When these artefacts are severe they can cause issues in image alignment during quantitative analyses. It has been suggested that higher scan speeds could decrease these drifting and distortion effects.[10]

In summary, SEM can be used to visualise the morphology of battery electrode materials; however, care must be taken in obtaining an accurate representation of the sample through

acquiring multiple images from many areas before attempting any quantitative assessment of the structural features on the electrodes, due to the relatively small sample areas analysed with this technique. Although a powerful technique for visualising the microstructure of the electrodes in LIBs, to gain further insight into structural and chemical changes of electrodes, such as the cracking of graphite particles, complementary tools such as Raman spectroscopy should be employed.

3.2.Raman spectroscopy

Raman spectroscopy provides spatially resolved chemical and structural information and can be operated both in *post-mortem ex situ* studies (which are the focus of this paper), as well as *in situ* during electrochemical cycling with the use of specially designed cells.[18] For LIB electrodes, Raman spectroscopy can be used to identify phase changes,[19] state of charge (SOC), cation mixing,[20] stress/strain (e.g. due to calendaring), electrolyte concentration, and short-range crystallinity, as well as the level of disorder, particle lateral size, and stages of lithium intercalation for graphitic components.[21]

Raman spectroscopy is, however, not normally suitable for the study of SEI composition, due to the weak Raman signal generated by the thin SEI and CEI layers. It is worth noting that this limitation may be overcome using surface enhanced Raman scattering techniques, which can detect surface species such as Li_2CO_3, $ROCO_2Li$, Li_xPO_y and $LiOH{\cdot}H_2O$,[22] or shell-isolated nanoparticle-enhanced Raman spectroscopy (SHINERS),[23] though these techniques are outside of the scope of this review.

The main advantage of Raman spectroscopy compared to the other techniques described herein is the ability to rapidly provide information regarding the short-range crystalline structure of electrodes, which can be used to evince degradation mechanisms such as particle cracking.[9] Although Raman spectroscopy is not generally considered a quantitative technique without

well-defined and traceable reference materials available for specific investigations, relative comparisons can be made between samples if a representative portion of the sample is analysed.

Prior to collecting Raman spectroscopy data, the potential for laser-induced damage must be assessed to avoid alteration of either the sample structure or chemistry. Reducing the beam power is the easiest way to minimise damage. However, this comes at the expense of lower signal-to-noise ratios and/or longer acquisition times. Users are recommended to analyse the same area with Raman spectroscopy performed with an increasing laser power incident at the surface, before measuring the same area with the lowest power again, and then to compare the spectra to confirm changes have not occurred due to the application of the laser (see Figure S3a). Previous studies have shown no sample damage for NMC-type materials with a laser power at the sample of up to 4 mW or a specific power of < 1 $mW/\mu m^2$.[24]

An important measurement challenge in the analysis of LIB electrodes with Raman spectroscopy is the highly heterogenous nature of the electrode structure and chemistry. Raman active species generally include metal oxides from NMC particles (peaks in the region: 300-700 cm^{-1}) and graphitic components from both carbon black and graphite: approximately 1350 cm^{-1} (D-peak), 1580 cm^{-1} (G-peak), 1620 cm^{-1} (D'-peak) and 2700 cm^{-1} (2D peak). To demonstrate this, we investigated the graphitic components in both NE and PE samples using Raman spectroscopy (see Figure 2 and Figure S3) and analysed the intensity ratio of the D-peak to the G-peak (I_D /I_G), which is known to correlate to the amount of disorder present in the graphitic lattice.[25] Examples of peak fitting for both NE and PE samples are reported in Figure S3.

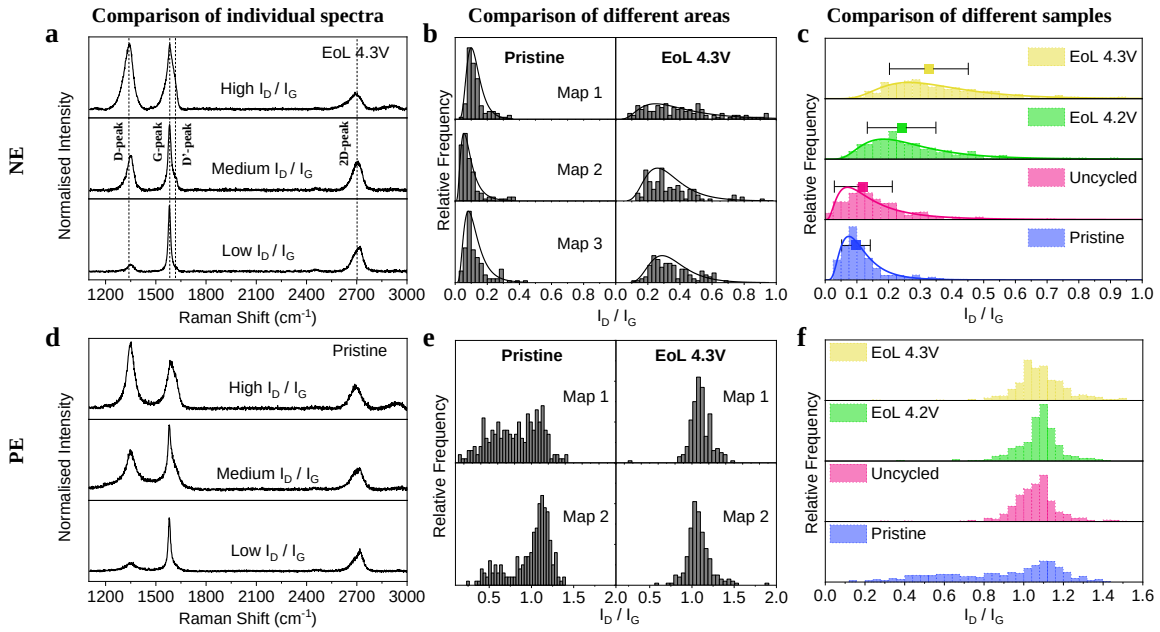

Figure 2. Analysis of graphitic components in NE (a-c) and PE (d-f) samples. a,d) Individual Raman spectra showing differences within samples (chosen to show extremes); b,e) Histograms of I_D/I_G ratios showing different areas of the samples for pristine and EoL 4.3 V NE and PE samples; c,f) Histograms of I_D/I_G ratios combining all spectra for each sample, in which c) was fitted with a lognormal distribution and lognormal median and standard deviation values have been inserted as points.

The high degree of inhomogeneity observed using Raman spectroscopy for graphitic components in the same sample is revealed through individual spectra collected from both the NE and PE, shown in Figure 2a and Figure 2d. To obtain a representative assessment of these electrodes, ≥ 100 spectra over a significant area of the sample (tens of micrometres in size) should be collected using Raman mapping across several regions of the sample. An example of a suitable number of spectra for the samples studied herein include Raman maps collected for NE samples (three 50 µm × 50 µm areas of each sample, total of > 350 spectra) and for PE samples (two 70 µm × 70 µm areas of each sample, total of > 450 spectra), where Figure 2b and 2e show the distribution of the I_D /I_G peak intensity ratios between different areas of pristine and EoL 4.3 V NE (Figure 2b) and PE (Figure 2e) samples. Note that, for carbon materials, the highest point of the peak is typically used as the intensity of the D- and G-peaks (rather than

the peak area) to quantify the level of disorder. This is due to the difficulties in determining the size of the D'-peak in disordered carbon materials, which can reduce the accuracy of the calculation of the area of the G-peak, as shown in Figure 2a and Figure S3.

Figure 2c,f show the statistical variation of the I_D /I_G ratio across the 4 samples of each type of electrode. From Figure 2c, a significant increase in the median I_D /I_G ratio was observed in cycled NE samples (EoL 4.2 V and EoL 4.3 V). The increase in the I_D/I_G ratio in these NE is due to an increase in the disorder of the graphitic lattice, potentially revealing that graphite particles are cracking and hence more lattice edges (and therefore disorder) are created. From Figure 2 and Figure S4 the inhomogeneity of the samples is clear, with a large range of I_D/I_G ratio values across several individual Raman maps of each type of sample. These data show that although there are still areas of the sample that are no more defective than the pristine electrode, there are more areas of increasing disorder for cycled electrodes. Higher average I_D/I_G ratio values are observed for electrodes cycled to higher voltages or for a greater number of cycles.

The uncycled NE samples exhibited fluorescence in the raw spectra, likely associated with residual electrolyte, which resulted in an inability to separate the Raman signal from the fluorescent background. Fluorescent backgrounds could be minimised by choosing alternative excitation wavelengths or by using stimulated Raman scattering.

Raman peaks related to the conductive carbon present in the PE samples (Figure 2d, e, f) exhibited a higher I_D/I_G ratio than that due to the carbon present in the NE samples. The PE sample results are indicative of a disordered type of carbonaceous material.[26] The average I_D/I_G ratios are significantly increased for the uncycled and cycled samples compared to the pristine samples, which could be indicative of degradation phenomena involving the conductive carbon

in the PE, such as de/intercalation reactions or particle cracking, or could be due to residual electrolyte causing formation of a carbonaceous layer on the electrodes.

While for graphitic components the interpretation of Raman spectra is relatively well-documented and understood in the literature, for the Raman-active components of NMC electrodes, challenges remain due to complex vibrational mode structures and a relatively weak Raman scattering cross-section, as shown in Figure 3a,b and Figure S5.

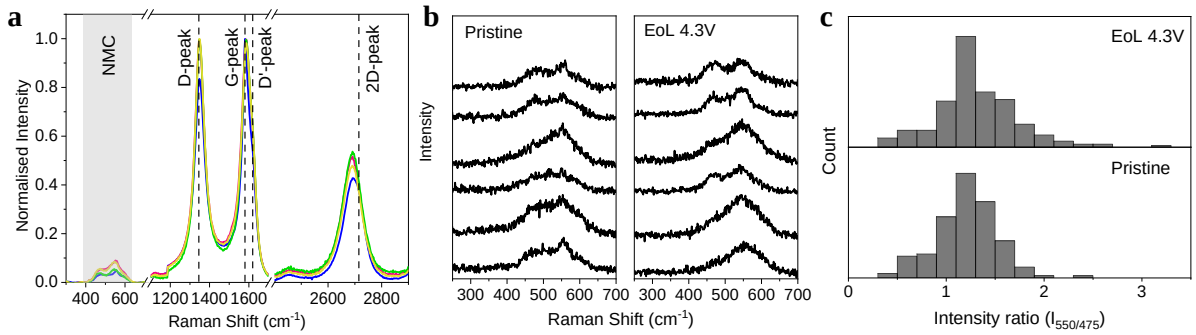

Figure 3. a) Averaged Raman spectra across maps of different samples of PE material, showing the main Raman-active components, including low intensity NMC peaks; b) individual spectra from pristine and EoL 4.3 V electrodes showing heterogeneity in the NMC region; c) histograms showing intensity ratio of NMC region peaks at points 550 cm^{-1} and 450 cm^{-1} for pristine and EoL 4.3 V electrodes.

Metal oxides such as NMC should yield two vibrational bands deriving from the M-O (M=metal) symmetrical stretching (A_{1g}) and O-M-O bending (E_g) vibrations.[27,28] However, clear interpretation is difficult because studies describing peak deconvolution, shifts, and broadening are often contradictory. A number of literature studies have deconvoluted the two broad peaks in the NMC region into a total of 6 peaks assigned to the oxides of the 3 metals present: Ni (~550 cm^{-1}, ~475 cm^{-1}), Co (~530 cm^{-1}, ~515 cm^{-1}) and Mn (~620 cm^{-1}, ~585 cm^{-1}).[19,29,30] However, additional studies (including density functional theory phonon calculations) have demonstrated that the presence of multiple metal oxides introduces complex lattice distortions, resulting in broader peaks due to multiple oxygen environments.[31,32] The relatively

broad peaks observed for NMC materials cannot simply be deconvoluted into peaks associated with individual metal oxides, because NMC is not a phase-separated mixture. Nevertheless, a band centred at ~609 cm^{-1} is observed experimentally in manganese-containing oxides and increases with increasing manganese content in lithiated compounds, which suggests that this vibrational mode could specifically arise from MnO_6 octahedra.[31,32] However, it has been noted that lithium vacancies may produce a Raman-active mode at ~600 cm^{-1} which would be difficult to resolve from the ~609 cm^{-1} feature.[31]

Some peaks in the NMC region (not observed in this work) have been associated with phase changes or SEI components. For example a band between 615 cm^{-1} and 685 cm^{-1} was assigned to cubic spinel phase formation,[19,33] a peak at 494 cm^{-1} was assigned to Ni-O in rock salt phase, and a small peak at 408 cm^{-1} was identified as LiF.[33] Changes in intensity ratio or shifts of the individual NMC peaks have been attributed to changes in SOC or cation mixing. It has been suggested that a higher intensity ratio of A_{1g}/E_g is indicative of higher SOC (higher lithiation) and lower cation mixing,[20,27] while a shift of the individual NMC Raman bands (A_{1g} and E_g) to lower frequencies has also been reported during delithiation.[34]

Therefore, interpretation of structural/chemical changes in NMC materials using Raman spectroscopy is not trivial. Moreover, samples exhibit large inhomogeneities in the NMC spectral region (see comparison of individual spectra in Figure 3b). The intensity ratio for the feature containing the associated NMC peaks was calculated for all spectra after background subtraction, using the intensity at 550 cm^{-1} and 475 cm^{-1} (see SI for details), and a comparison between different samples is shown in Figure 3c and Figure S5. Although this relatively crude type of analysis may not be entirely appropriate due to the many unknowns, this method can be used to show variations in the NMC structure both within one sample and between different samples. While a large variation of this intensity ratio is evident in each individual PE sample, when a statistically relevant number of spectra are analysed no significant change between the

different samples is observed, suggesting that Raman spectroscopy may not distinguish differences in NMC structure through *post-mortem* studies, in contrast to the analysis of the graphite NE material. Therefore, other complementary techniques are required to understand variations in NMC chemistry between cycled electrodes.

3.3.X-ray Photoelectron Spectroscopy (XPS)

XPS is a quantitative analysis technique for measuring the elemental composition and chemical environment at the surface of materials, typically within ~10 nm of the surface. It is commonly used in LIB research as a *post-mortem* technique to quantitatively assess the surface chemistry, particularly the SEI and CEI, of battery electrode materials.[35–38] It has also been used to ascertain the oxidation state of metal ions in the PE,[39] determine active material stoichiometry, lithium distribution (with depth profiling),[40] as well as to identify impurities and contaminants with a detection limit between ~1 at% (for light elements) and better than 0.01 at% (for heavy elements). Despite XPS measurements being well standardised, a recent meta-analysis performed by Major *et al.* on three respectable journals over a six-month period showed that approximately 30 % of general XPS analyses were sufficiently flawed to call into question the validity of the conclusions of the paper.[41] With greater sample complexity comes an analytical landscape full of pitfalls, so it should be no surprise that obtaining reproducible data for LIB materials is often challenging. Analysing SEI and CEI composition presents some additional challenges: (i) many elements in the SEI have similar binding energies, so peaks are often overlapping;[42] (ii) the SEI is electrically insulating and sample charging causes energy shifts in photoelectron peaks;[38,42] (iii) X-rays, charge neutralising electrons, or Ar^+ ions used for sputtering can potentially alter the chemistry of the sample;[38,40,43] (iv) it is difficult to define the sputtering depth in a depth profile because of differential sputtering rates from the phase-separated components,[40] (v) the chemistry of the SEI/CEI is highly reactive and sensitive to

the environment so for *ex situ* techniques sample handling (e.g. inert transfer) is an important consideration.

Figure 4a shows the variability of chemical assignments for some candidate lithium- and fluorine-containing SEI compounds in the literature (e.g. LiF, $LiPF_6$, Li_2O, LiOH, Li_2CO_3, etc.) using the reported binding energy positions of the Li 1s and F 1s peaks, i.e. E_{Li1s} and E_{F1s}, respectively. The LIB-related literature binding energies shown in Figure 4a for some of the species identified in the SEI are reported in Table S4. Large binding energy shifts in peak positions have been widely documented for XPS on NE materials.[42,44] These shifts are mostly associated with the electrically insulating nature of the SEI, causing the surface to charge.[42] Differential charging also occurs for different compounds in the sample, depending on their conductivity and electron emission rates, meaning that peaks from different phases, spatial locations, or depths of the sample can shift by different binding energy values.[42] The state of charge of the electrodes and gradients in Li concentration have also been correlated to charging effects.[44,45]

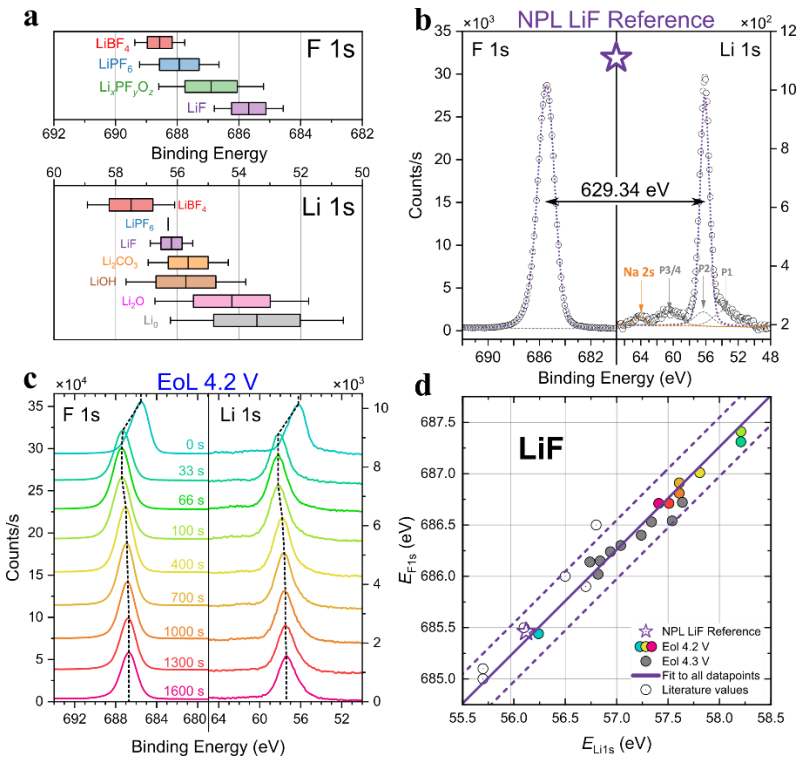

Figure 4. (a) The range of XPS binding energies reported in LIB-related literature for relevant Li-containing chemical environments. The black solid line of each range is the mean binding energy value, while the box and whiskers show the range of binding energies for each chemical environment up to 1 standard deviation (σ) and 2σ respectively. (b) Reference spectra of F 1s and Li 1s acquired from a LiF reference material in this work. (c) F 1s and Li 1s spectra acquired from the EoL 4.2 V NE during a depth profile using 5 keV Ar^+ ions with sputter time labelled for each spectrum. (d) E_{F1s} vs E_{Li1s} for the NPL LiF reference, EoL 4.2 V (coloured relative to (c)) and EOL 4.3 V (see Figure S6g) NE depth profiles, and LiF reference values from literature. The solid purple line represents a linear fit with a slope of unity and an intercept of ΔE = 629.27 eV. The dashed purple lines represent the 2σ uncertainty of the intercept which is ± 0.29 eV.

Despite efforts to control surface charging (see SI for details), Figure 4a shows that there is demonstrable lack of reproducibility in binding energy assignments between different studies for the same chemical state. Some chemical assignments, such as LiF, have a narrower range of reported values compared to LiOH, Li_2O, or Li metal, but E_{Li1s} and E_{F1s} still vary by ~1.4 eV and ~2.4 eV, respectively, and exhibit significant overlap with other compounds such as Li_2CO_3. This makes confident peak assignment difficult and may lead to an incorrect interpretation of the chemical environment of LIB materials. Based on this analysis, the assignment of compounds from the Li 1s position alone and using a single literature reference is highly questionable. It is therefore vitally important that XPS analysts verify the binding energy positions of some common chemical environments found in battery materials by acquiring spectra from suitable reference materials.

Figure 4b shows high-resolution spectra of the F 1s and Li 1s peaks acquired from a polished LiF optical window (Crystran, Poole, UK) which was used as a reference sample (and labelled "NPL LiF reference"). The F 1s and Li 1s peaks are observed at 685.46 eV and 56.12 eV, respectively (when energy referenced to adventitious carbon at 285.0 eV), and the F 1s peak exhibits a single component indicative of the expected chemical state. Conversely, the Li 1s lineshape appears to contain several minor components which could erroneously be interpreted as different chemical states. In fact, these features are the electron energy loss structure from

the nearby F 2s peak.[46] Such insights into the expected lineshape of a photoelectron peak are vital for peak fitting and for determining precise stoichiometries. Other lithium- and fluorine-containing species, such as polyvinylidene fluoride (PVDF) and Li_2CO_3, were also analysed and employed as reference materials, as shown in Figures S6e and S6f, respectively. Spectra acquired for Figure 4b required energy referencing because the LiF surface exhibited charging and therefore necessitated the use of a charge neutraliser during measurement. The stated binding energies are energy referenced to the adventitious carbon peak at 285.0 eV because there is no other suitable internal reference. However, given that adventitious carbon may also exhibit a wide binding energy range depending on the surface on which it is adsorbed, the uncertainty in the positions of the Li 1s and F 1s peaks is much higher (~ ±1 eV) than indicated. The two decimal place reporting of peak position relates to the precision of the peak position measurement. The purpose of retaining this precision is the use of a relative peak energy scheme proposed for LIB materials by Wood and Teeter.[42] This approach uses the binding energy differences (ΔE) between photoelectron peaks originating from the same chemical state, a value which is unaffected by charging-induced shifts, as opposed to absolute positions, which are affected by charging.

Figure 4c shows the F 1s and Li 1s peaks from the SEI of the EoL 4.2 V NE sample during a depth profile with monoatomic Ar^+ sputtering. All spectra have been energy referenced to the graphitic C 1s component at 284.4 eV, yet, despite this, significant energy shifts are observed. The maximum intensity peak positions for both the F 1s and Li 1s peaks (E_{F1s} and E_{Li1s}, respectively) in Figure 4c, are plotted in Figure 4d, along with data from an identical experiment on the EoL 4.3 V NE sample, the NPL LiF reference sample from Figure 4b, and literature values for other LiF reference materials (Table S4). Figure 4d demonstrates that a wide range of E_{F1s} and E_{Li1s} can be attributed to LiF. By fitting these datapoints with a linear regression (fixing the slope at unity), we determine a mean ΔE of 629.27 eV with a 2σ

uncertainty of ± 0.29 eV. This is a significant improvement in uncertainty compared to the range of absolute binding energies reported in LIB-related literature. This approach works well in differentiating the compounds of lithium and when used with appropriate stoichiometric ratios and constraints informed by suitable reference materials. Nevertheless, caution is needed when studying LIB materials as multiple differentially charged Li-containing phases will result in complex lineshapes that are difficult to analyse, even with this method.

In contrast to NE materials, we observed that PE materials are usually sufficiently conductive that surface charging is minimal, due to the thinner CEI layer. It was found that a well-optimised charge neutralisation procedure is sufficient to mitigate surface charging for the CEI. Subsequently, peak position shifts due to surface charging may be corrected by using a specific component as an internal energy reference, e.g. the $\underline{C}F_2$ component of the C 1s core level spectrum from the PVDF binder (290.7 eV). Nevertheless, care should be taken to ensure that the charge neutralisation methodology applied to NE samples should also be applied to PE samples because the CEI is an insulating inhomogeneous structure, like the SEI.

Figure 5a displays survey spectra of the pristine NMC PE before (blue) and after (green) sputtering with 5 keV Ar^+ ions for 500 s. Also shown is a survey spectrum acquired from a pellet of NMC 811 powder (red) after sputtering with 5 keV Ar^+ ions for 1200 s. Survey spectra acquired before and after sputtering the uncycled and EoL electrodes are shown in Figures S8a to S8c. Before sputtering, the pristine PE survey scan predominately shows F, O, and C related to the PVDF binder and carbon black matrix. This matrix, as well as inorganics such as Li_2CO_3, forms overlayers that attenuate the photoelectron signal from the NMC metal core levels, often to the point that they are undetectable. This not only results in large uncertainties in the calculated atomic fractions of the metals, but also leads to a quantification that does not accurately represent the bulk of the PE material; note that the spectrum for the pristine PE

before sputtering bears no resemblance to the reference NMC 811 powder spectrum. It is therefore necessary to utilise Ar^+ ion sputtering to remove the overlayer material to achieve more representative spectra.[8] It should be noted that the process of sputtering, as well as the use of X-ray and electron sources, has been reported to alter the surface chemistry, as discussed in the SI. Furthermore, due to the inhomogeneity of the electrodes and the CEI (or SEI for the NE), there is variability in the sputtering depth as some compounds such as organic species are preferentially sputtered (see Figure S7 for an example).[40] Profilometer studies have been used in the literature to determine the sputter depth of different species and it was observed that organic compounds were sputtered at higher rates than inorganic salts, which has the effect of increasing surface roughness.[40]

In Figure 5a, in the 'After Sputtering' survey (green), the characteristic and complex photoelectron signal related to the NMC metals is revealed at binding energies between 1000 eV and 500 eV. Considering the binding energies of the most intense photoelectron core level from each metal: Ni 2p (3/2 at ~853 eV), Mn 2p (3/2 at ~639 eV), and Co 2p (3/2 at ~778 eV), another measurement challenge becomes apparent. For spectra acquired using Al Kα X-rays (the most ubiquitous X-ray source energy in commercial XPS systems), the transition metals have significant Auger photoelectron signal across the same range of binding energies. Most notably, the Ni LMM Auger structure dominates and makes accurate area determination of the Mn 2p and Co 2p peaks extremely difficult. Additionally, the Ni 2p peak significantly overlaps the F KLL Auger peak, which may lead to an overestimation of the Ni content due to the additional intensity of the F KLL Auger peak. This becomes an issue when considering NMC PE with fluorine-containing binders; indeed, misidentification of the F KLL as a nickel-containing chemical species has occurred in the literature.[47,48,49] XPS has been used to provide quantitative information on the oxidation states of metals in NMC (e.g. Ni^{2+}/Ni^{3+} ratio), which is particularly important in nickel-rich NMCs where cation mixing occurs in the

presence of Ni^{2+}.[39,50] However, measuring the relative concentrations of chemical states of metals through peak-fitting of XPS spectra is non-trivial, due to asymmetric peaks, complex multiplet splitting, shake-up and plasmon loss features, similar or uncertain binding energies of multiple components, and chemical damage due to Ar^+ sputtering.[39] A lack of pure reference materials for Ni^{3+} also complicates these efforts, as discussed in the SI.

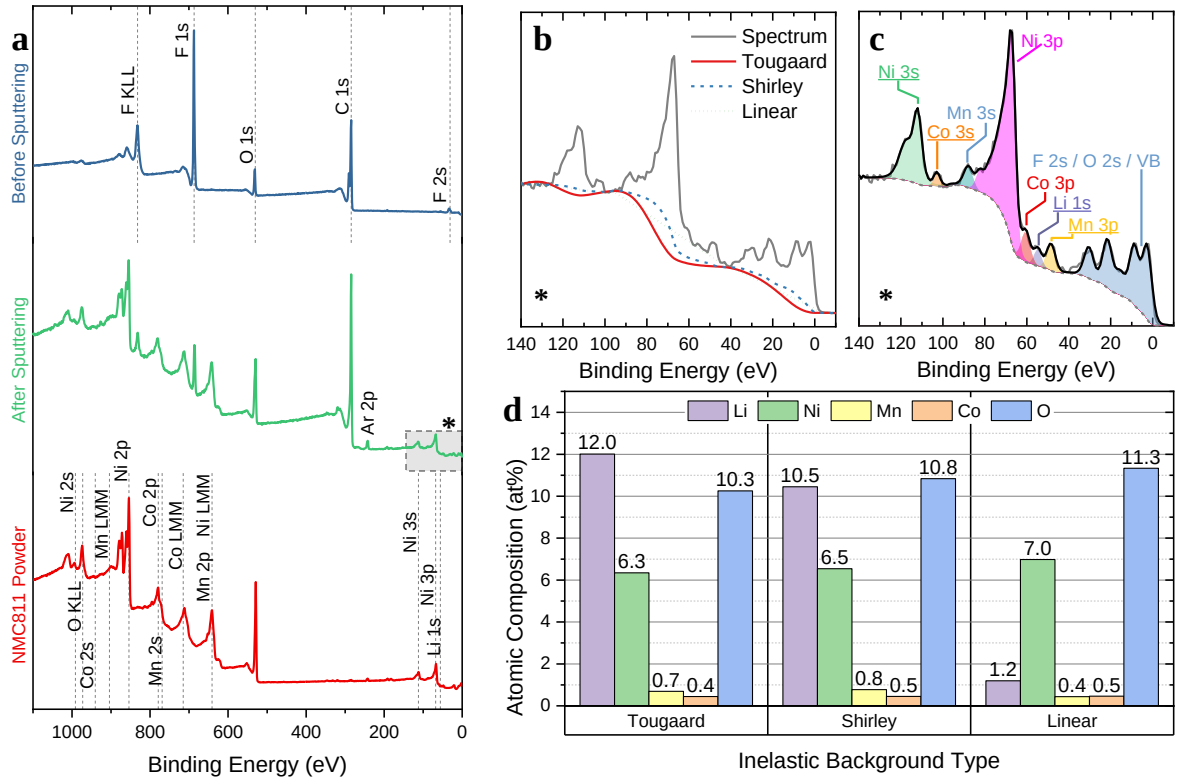

Figure 5. Survey spectra of the pristine PE before and after sputtering alongside a reference spectrum of NMC 811 powder. (b) Tougaard, Shirley, and linear inelastic background algorithms applied to the low binding energy region (140 eV to 0 eV) of the survey spectrum acquired on the pristine PE after sputtering. (c) Constrained peak fitting model of the low binding region shown in Fig. 6b showing core levels related to Ni, Mn, Co, and Li, which can be used in quantification. (d) Quantification of the pristine PE using different inelastic backgrounds and the same low binding energy core levels. Only the atomic composition of the main NMC 811 elements is shown, i.e. Li, Ni, Mn, Co, and O.

Figure 5b and c display the low binding energy region (140 eV to –10 eV) of the survey spectrum after sputtering shown in Figure 5a by the shaded grey region. Figure 5b demonstrates the impact of using the most common background algorithms over this region: Tougaard, Shirley, and linear. Figure 5c shows a peak fitting model used on this region to extract the atomic composition using a Shirley background. This region contains core levels from all the NMC metals and the Li ions, allowing a determination of the full $LiNi_xMn_yCo_zO_2$ stoichiometry. There are several advantages of using this region for quantification. First, the range of kinetic energies of the photoelectrons emitted from the core levels of interest is reduced, therefore minimising quantification errors arising from energy-dependent escape depth and analyser transmission differences. Second, there are no Auger electron features which overlap the photoelectron peaks, simplifying the peak fitting model. Unfortunately, this region has a much lower absolute count rate, which therefore requires longer acquisitions to achieve an acceptable signal-to-noise ratio. Figure 5d shows the atomic composition for Li, Ni, Mn, Co, and O of the pristine PE after sputtering. The peak areas used for quantification have been extracted from the Ni 3s, Co 3s, Li 1s, Mn 3p, and O 1s peaks. The same peak positions, sensitivity factors and transmission function have been used in each case; the only difference is the choice of inelastic background algorithm. The peak model constraints and background algorithm parameters are detailed in the SI. The atomic composition for the uncycled and EoL electrodes using a Tougaard background are shown in Figure S8d. The Tougaard and Shirley quantifications give a transition metal relative composition of ~$Ni_{0.85}Mn_{0.09}Co_{0.06}$ and the linear quantification gives a relative composition ~$Ni_{0.89}Mn_{0.05}Co_{0.06}$. Considering that the uncertainty in the atomic fraction for the values under 1 at% (Mn and Co) may be as large as the stated at%,[51] we conclude that the NMC ratio given by these quantifications is, within uncertainty, consistent with the expected NMC stoichiometry of the pristine PE, $Ni_{0.80}Mn_{0.10}Co_{0.10}$. Determination of the metal content in NMC materials has also been used in

the analysis of metal dissolution.[52,53] As changes in atomic fraction of transition metals may be on the order of the XPS limit of detection,[54] the uncertainty (which is largely due to the data analysis) may be larger than the measured at%.[51] However the precision of XPS (which is inherent to the measurement) may be sufficient to detect a change if a robust and consistent peak analysis has been utilised over multiple repeat spectra.

Quantifications using the Tougaard and Shirley backgrounds appear to agree well in terms of lithium concentration. The Tougaard background quantification gives ~2 at% more Li than the Shirley background quantification and both provide an approximate Li:O stoichiometry of unity. In comparison, the linear background results in a significantly lower lithium content, which is due to the linear background underestimating the area under the Li 1s peak, as shown in Figure 5b. Determining the lithium content and distribution in LIB materials is important in order to understand their charge-discharge characteristics, so ambiguities in lithium content are concerning. In this case, the linear background quantification also yields inconsistent atomic fractions for the same element, e.g. the intensity of the Co 3p peak should be ~2.4 times that of the Co 3s peak (using NPL sensitivity factors) but is underestimated when using the linear background. Selecting an appropriate background algorithm and applying it consistently is therefore vital, and linear backgrounds should only be used when the decay of the inelastic background to lower kinetic energies is dominant.[55] Analogous to the linear quantification described above, a similar Li depletion will be inferred if, during analysis, the boundary conditions of the Li 1s peak area integration are too narrow or not adjusted for changes in peak energy. The potential migration of Li ions away from the surface during Ar^+ ion sputtering should also be considered. The process of ion migration due to sputtering is well documented.[56] In the case of LIB electrodes, positive ions implant into the sample surface and their charge repels mobile Li^+ ions into the bulk of the electrode. This may result in an underestimation of

the Li atomic fraction if it is not accounted for. The mobile Li^+ may also accumulate at interfaces within layered materials when it cannot penetrate the underlying material.[57]

The issues of Li^+ migration may be avoided by using high-energy small-size Ar clusters (e.g. 20 keV Ar_{500}), which can be used to depth profile through inorganics without implanting Ar^+ into the surface.[57] In many materials, damage to freshly exposed surfaces may be reduced or eliminated by using Ar clusters in preference to monoatomic Ar^+ ions, so this approach may help preserve the chemical state of the active material.[58] However, the issues of preferential sputtering remain, and the etch rate is significantly lower than monoatomic Ar^+ sputtering, potentially leading to untenable experiment times. There is one potential way to avoid sputtering altogether. Hard X-ray photoelectron spectroscopy (HAXPES) has an information depth larger than XPS due to the increased path length of high energy electrons. It permits the measurement of higher energy core levels which often resolves the problems of overlapping peaks discussed previously.[59] As well as allowing elemental composition and chemical state information from a greater depth, which has the advantage of avoiding sputtering induced damage altogether,[45] recent studies have shown that quantitative analysis of the inelastic background can detect buried layers and measure their depth.[60] HAXPES has been especially useful for characterising solid state LIBs, CEI/SEI formation, and degradation processes with greater bulk sensitivity.[35,45,61] Whilst it has long been a technique predominately used at synchrotron facilities, HAXPES is more accessible as laboratory based commercial instruments using Ag (Lα = 2.98 keV), Cr (Kα = 5.42 keV), and Ga (Kα = 9.25 keV) sources become available.[59]

3.4. Time of Flight Secondary Ion Mass Spectrometry (ToF-SIMS)

Another widely employed chemical measurement technique is ToF-SIMS, which can provide spatially resolved chemical information about battery electrodes. ToF-SIMS can be used to

study metal dissolution through the detection of re-deposited metal ions in the SEI,[52] or through changes in metal concentration or distribution in NMC electrodes (e.g. reduction of secondary metal ion intensity at the surface), which may or may not be indicative of metal dissolution phenomena.[36,52] ToF-SIMS can also be used for analysis of the SEI and CEI composition,[17] and to study the location of lithium species and metal oxides.[62]

ToF-SIMS is a surface sensitive technique but, like XPS, can access bulk material with the use of a sputtering beam. Whilst not quantitative, relative quantification can be achieved with suitable normalisation or reference materials. ToF-SIMS exhibits some advantages over XPS, including higher spatial resolution (which enables the study of the distribution of chemical species through surface imaging or 3D reconstructions) and generally higher sensitivity (ppm, depending upon ionisation probabilities which, on the other hand, vary strongly). A higher spatial resolution allows the detection of changes in local chemistry. For example, it has been shown that the composition of an SEI present on the surface of graphite was different when formed on basal planes (mostly organic compounds) compared to that formed on edge planes (mostly inorganic compounds containing lithium and fluorine).[63] The high sensitivity of ToF-SIMS also permits detection of changes in metal oxide composition that cannot always be detected in XPS, as they can be close to instrument detection limit,[64] or changes in local chemistry.

It should be noted that in this study, we use a two different ToF-SIMS instruments, one that uses a 10 keV Cs^+ sputter beam and another with a similar configuration except that a 20 keV Ar_{2000}^+ sputter beam is used instead, as shown in Figure 7. 3D secondary ion intensity maps for SEI components (PO_3^- and F^-) and bulk material (C_2^-) for pristine, uncycled and EoL NE and PE samples are shown in Figure 6a. Analysis was conducted using a 25 keV Bi_3^+ analysis beam with a 100 μm × 100 μm field of view and with 10 keV Cs^+ sputtering for 600 s. Further

analysis of a separate portion of the same sample (collected from a nearby area) was conducted using 20 keV $Ar2000^+$ sputtering for 300 s (ToF-SIMS V instrument). Strong heterogeneity in the spatial distribution of the SEI and CEI components is observed from the 2D secondary ion intensity maps (Figure 6b). These are constructed by summing intensities for each pixel over all depths. Measurement details are provided in the SI. Pristine electrodes display mainly carbonaceous species on the surface, thought to derive from the binder and, for the NE, active material. Uncycled electrodes show a higher quantity of fluorine (F^-) and phosphorous-containing species (PO_3^-) assigned to SEI components. After cycling the electrodes to their EoL at different voltages, a change in surface chemistry is observed with higher ratios of fluorine to phosphorous species compared to the uncycled electrode, suggesting a change in SEI composition.

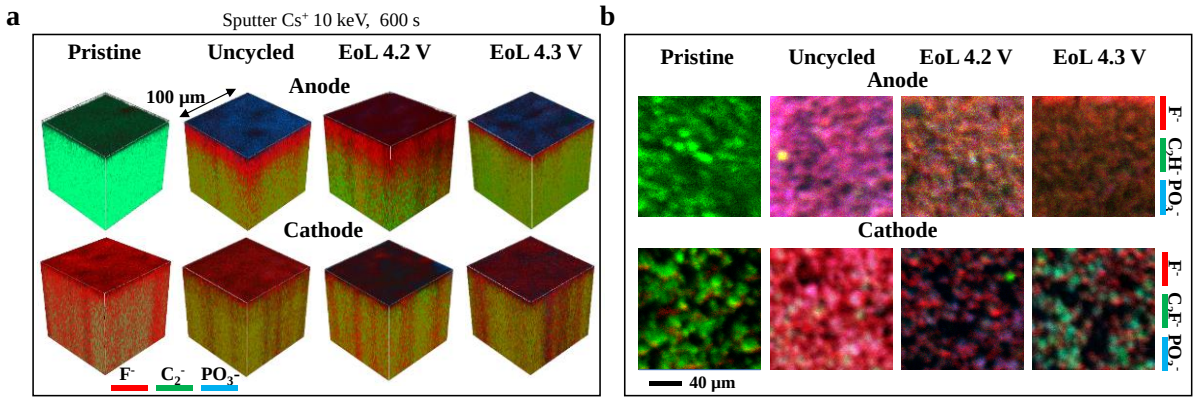

Figure 6. SEI and CEI spatial distribution. a) secondary ion 3D render for F^-, C_2^- and PO_3^- from sputtering with Cs^+ at 10 keV for 600 s; b) 2D images from depth profiles for F^-, C_2H^- or C_2F, and PO_3^- from sputtering with Ar_{2000}^+ at 20 keV for 300 s.

In order to study potential metal dissolution, the intensity ratios of metal oxide ions were also plotted in Figure 7. The 2D data derives from summing in depth (Figure 7a) over a 3D volume and shows similar heterogeneity to previously characterised ions in Figure 6. The intensity ratios of MnO_2^- to CoO_2^- (Figure 7b) and NiO_2^- to CoO_2^- (Figure 7c) with sputter time (depth)

show significant reduction for the EoL 4.2 V and EoL 4.3 V samples. This is evidence for manganese and nickel dissolution during electrochemical cycling.

Nevertheless, the intensity of secondary ions as a means of assessing concentrations should be treated with caution. The secondary ion intensity is strongly dependent on so-called matrix effects (i.e. local chemistry changes the ionisation probability).[65] Signal intensity can vary as a result of sputtering yield (i.e. low mass and low binding energies result in high sputtering yield), edge effects (i.e. change in sputtering yield due to topography)[66] and moreover, the absolute and relative intensities of secondary ions change when different primary ions and energies are used. Care should be taken to ensure that the instrumentation is operating within an appropriate regime: for example, the SIMS sensitivity to Li^+ is very high and the signal can easily saturate a time-of-flight detector.[62] Efforts have been made to derive quantitative information from ToF-SIMS, for example the lithium concentration in NMC-type electrodes, by performing a calibration to account for edge and matrix effects.[67] However, due to large morphological and chemical inhomogeneities of these samples, there is still significant uncertainty and further metrological work is required.

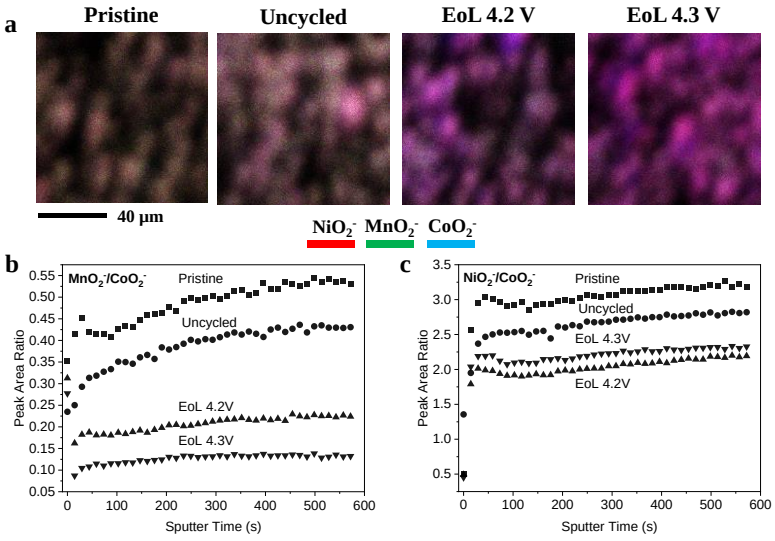

Figure 7. Metal dissolution on PE electrodes. a) RGB overlay 2D images constructed by summation over all sputter times showing 3 secondary ions from metal oxides; b) intensity ratio of MnO_2^- to CoO_2- with sputtering time and c) intensity ratio of NiO_2^- to CoO_2^- with sputtering time.

Similar to XPS, another effect that must be accounted for is preferential sputtering. Profilometer studies have been performed on NMC electrodes to quantify the sputtering yield and highlighted an increase in surface roughness in the sputtered area due to preferential removal (2-2.5 times) of polymeric binder/carbon additive compared to that of the NMC active material.[68] The sputtering yield and the difference in sputtering yield between materials also varies with the energy and type of primary ion beam source.[43]

One strength of ToF-SIMS in comparison to XPS is the higher sensitivity to lithium and the capability to detect hydrogen.[63] Energy dispersive spectroscopy (EDS), often performed in combination with SEM, can also obtain high spatial resolution but cannot detect lithium.[67] However, when employing ToF-SIMS to investigate the location of lithium we must consider that lithium ions could potentially re-distribute during cell disassembly or due to forward recoil in sputtering.[62] As discussed previously for XPS, ion sputtering beams or primary ion beams can also cause the migration of highly mobile lithium ions during analysis,[69] but it has been proposed that lithium ion migration could be minimised at lower temperatures.[69] Moreover, assignment of secondary ion fragments to specific chemistries is not trivial, due to the multiple lithium-containing compounds in both the SEI/CEI and active material.[17,43] Generally Li^+ ions are used to characterise distribution of lithium species in electrodes; however, it has been proposed that Li^- ions could instead be employed for graphitic electrodes.[70] The authors suggested that Li^- ions could be more easily ionised on the surface of graphite electrodes, due to its conductivity and capability of supplying electrons.

One potential approach to distinguish different species is the use of isotope labelling, for example to differentiate between lithium intercalating the PE and lithium deriving from the electrolyte.[17] Reference materials can also be employed to identify ions specific to one chemical, although the ion intensities may vary depending on the surrounding chemical environment (matrix).[62]

4. CONCLUSIONS

Understanding LIB degradation mechanisms is critical to improving their performance and lifetime. However, for such complex systems no one technique alone can provide a full picture of structural and chemical changes occurring during battery degradation. Multiple techniques are required to gain a comprehensive understanding and we have demonstrated in this work that *post-mortem* characterisation of LIB electrodes is not trivial and may result in unreliable data. We have focused our discussion on the measurement challenges and solutions with examples of analyses performed on real-world LIB graphite NEs and NMC PEs. We propose best practice guidelines to promote the accurate and reproducible characterisation of LIB electrodes and ensure results are comparable across the research community. To this end, essential recommendations for each of the techniques discussed are summarised below:

4.1. Measurement guidelines

4.1.1. General guidelines

- To improve reproducibility across different laboratories, report the sample harvesting technique used to prepare the samples for surface analysis and provide as much detail as possible on the history of the sample. For example, state whether the samples were rinsed and with what solvent.

- Use inert atmosphere transport systems for LIB material samples. Some instrument manufacturers already have solutions to prevent material changes due to the interaction with ambient conditions.
- Due to the chemical inhomogeneities present in both the electrodes, for both spectroscopic and imaging techniques, acquire data from across multiple different areas of the samples. This allows a comparison of the areas analysed and ensures that the analysis is representative of the entire sample. For XPS and SIMS, Ar^+ ion sputtering may be used to remove signal attenuating overlayers or allow a depth profile through the SEI/CEI, but be aware of sputtering induced damage when using monoatomic modes. Gas cluster modes can mitigate sputtering damage and Li migration, at the cost of increased experiment times due to smaller etch rates.
- Be aware that some of the materials in LIB electrodes are preferentially sputtered when using ion beams so there is an associated difficulty in calculating sputter depth from sputter time. Also, consider issues such as ion migration due to sputter-induced redistribution processes, causing issues with the observed location or depth of chemical species.
- Do not solely rely on literature interpretation of spectroscopic assignments, especially for Raman spectroscopy and XPS investigations. Collect reference spectra of appropriate reference materials and compounds for techniques like XPS, SIMS, and Raman spectroscopy. Use these reference spectra to apply constraints to your data analysis and verify agreement (where possible) with literature.

4.1.2. FIB-SEM

- Be wary of imaging artefacts such as curtaining that can be introduced due to the different milling rates of the materials in these samples.
- Employ complementary techniques to ensure accurate conclusions about the structure of the electrodes.

4.1.3. Raman spectroscopy

- Assess and avoid laser induced damage by measuring the same area at increasing laser powers.
- Be wary of contradictory interpretation of NMC-related Raman peaks; *post-mortem* measurements may not be useful to compare different samples but will show heterogeneity within a sample.

4.1.4. XPS

- Determine the optimum charge compensation parameters for each new analysis area (and within reason, depth) on each sample. Isolating the sample from ground may allow greater control of the charge neutraliser and mitigate differential charging.
- Where possible, use relative binding energy differences between components in different core levels for chemical assignment, in conjunction with peak fitting constraints that preserve stoichiometric ratios and lineshapes from reference spectra.
- When determining atomic composition, use other non-overlapping core levels where possible. The low binding energy region between 140 eV and 0 eV can be used to determine the transition metal stoichiometry of the NMC PE.

4.1.5. ToF-SIMS

- Be aware that SIMS does not provide a quantitative assessment of complex materials such as LIB electrodes, but can be used to understand variations in chemistry within samples.
- Take precautions to ensure that the instrumentation is operating within an appropriate regime, for example that the Li^+ signal is not saturating the detector.
- Assign secondary ions to specific chemical species with caution for complex materials such as LIB electrodes with many components.

ASSOCIATED CONTENT

Supporting Information. Additional details on materials and methods for each technique, additional SEM and FIB-SEM images, example of fitted Raman spectra and complementary Raman spectroscopy data, additional XPS spectra of samples and reference materials, table with binding energy values for common SEI/CEI compounds, relative quantification, additional discussion on XPS measurement challenges.

The following files are available free of charge.

brief description (file type, i.e., PDF)

AUTHOR INFORMATION

Corresponding Author

* Email: sofia.marchesini@npl.co.uk; Phone: +44 20 8943 6587, ORCiD: 0000-0002-5051-0936

Present Addresses

[a] Current address: Microsaic Systems, GMS House, Boundary Rd, Woking GU21 5BX, United Kingdom

[b] Current address: Cambridge Enterprise, University of Cambridge, Cambridge CB3 0GT, United Kingdom

[c] Current address: Atlantic Technological University, Ballytivan, Sligo F91 YW50, Ireland

[d] Current address: Philips-Medisize Sligo Ltd, Rathedmond, Sligo, F91 YE92 Ireland

Author Contributions

The manuscript was written through contributions of all authors. All authors have given approval to the final version of the manuscript. **Sofia Marchesini**: Conceptualization,

Methodology, Investigation, Formal analysis, Writing - original draft. **Benjamen P. Reed**: Methodology, Investigation, Formal analysis, Writing – original draft. **Helen Jones**, **Lidija Matjacic**, **Timothy E. Rosser**, **Yundong Zhou**, **Barry Brennan**, and **Mariavitalia Tiddia:** Investigation, Formal analysis, Writing – Review & Editing. **Rhodri Jervis, Melanie. J. Loveridge**: Resources, Writing – Review & Editing. **Rinaldo Raccichini**, **Juyeon Park**, **Andrew J. Wain**, **Gareth Hinds**, **Ian S. Gilmore**, **Alexander G. Shard**, and **Andrew J. Pollard**: Conceptualization, Methodology, Supervision, Writing - review & editing.

Funding Sources

This work was funded by the UK Department of Business, Energy and Industrial Strategy (BEIS) through the National Measurement System (NMS) programme (#124739, Metrology for High Energy Density Batteries and #126101, Metrology and Standards for the UK Battery Value Chain). This work was supported by the Faraday Institution (EP/S003053/1) under grants FIRG001, FIRG028, and FIRG0024.

ACKNOWLEDGMENT

The authors would like to acknowledge Kratos Analytical Ltd (UK) for providing the inert sample transporter for XPS measurements.

REFERENCES

(1) *Faraday battery challenge: Industrial Strategy Challenge Fund - GOV.UK*. https://www.gov.uk/government/collections/faraday-battery-challenge-industrial-strategy-challenge-fund (accessed 2020-03-30).

(2) Schmuch, R.; Wagner, R.; Hörpel, G.; Placke, T.; Winter, M. Performance and Cost of Materials for Lithium-Based Rechargeable Automotive Batteries. *Nat. Energy* **2018**, *3* (4), 267–278. https://doi.org/10.1038/s41560-018-0107-2.

(3) Edge, J. S.; O'Kane, S.; Prosser, R.; Kirkaldy, N. D.; Patel, A. N.; Hales, A.; Ghosh, A.; Ai, W.;

Chen, J.; Yang, J.; Li, S.; Pang, M. C.; Bravo Diaz, L.; Tomaszewska, A.; Marzook, M. W.; Radhakrishnan, K. N.; Wang, H.; Patel, Y.; Wu, B.; Offer, G. J. Lithium Ion Battery Degradation: What You Need to Know. *Phys. Chem. Chem. Phys.* **2021**, *23* (14), 8200–8221. https://doi.org/10.1039/D1CP00359C.

(4) Pender, J. P.; Jha, G.; Youn, D. H.; Ziegler, J. M.; Andoni, I.; Choi, E. J.; Heller, A.; Dunn, B. S.; Weiss, P. S.; Penner, R. M.; Mullins, C. B. Electrode Degradation in Lithium-Ion Batteries. *ACS Nano* **2020**, *14* (2), 1243–1295. https://doi.org/10.1021/ACSNANO.9B04365.

(5) Chang-Hui Chen; Dominika Gastol; Ferran Brosa Planella; Kieran O'Regan; W. Dhammika Widanage; and Emma Kendrick. Development of Experimental Techniques for Parameterization of Multi-Scale Lithium-Ion Battery Models. *J. Electrochem. Soc.* **2020**, *167*, 080534. https://doi.org/10.1149/1945-7111/ab9050.

(6) Liu, H.; Wolf, M.; Karki, K.; Yu, Y. S.; Stach, E. A.; Cabana, J.; Chapman, K. W.; Chupas, P. J. Intergranular Cracking as a Major Cause of Long-Term Capacity Fading of Layered Cathodes. *Nano Lett.* **2017**, *17* (6), 3452–3457. https://doi.org/10.1021/acs.nanolett.7b00379.

(7) Lee, S. H.; You, H. G.; Han, K. S.; Kim, J.; Jung, I. H.; Song, J. H. A New Approach to Surface Properties of Solid Electrolyte Interphase on a Graphite Negative Electrode. *J. Power Sources* **2014**, *247*, 307–313. https://doi.org/10.1016/j.jpowsour.2013.08.105.

(8) Waldmann, T.; Iturrondobeitia, A.; Kasper, M.; Ghanbari, N.; Aguesse, F.; Bekaert, E.; Daniel, L.; Genies, S.; Gordon, I. J.; Löble, M. W.; De Vito, E.; Wohlfahrt-Mehrens, M. Review—Post-Mortem Analysis of Aged Lithium-Ion Batteries: Disassembly Methodology and Physico-Chemical Analysis Techniques. *J. Electrochem. Soc.* **2016**, *163* (10), A2149–A2164. https://doi.org/10.1149/2.1211609jes.

(9) Bhattacharya, S.; Riahi, A. R.; Alpas, A. T. A Transmission Electron Microscopy Study of Crack Formation and Propagation in Electrochemically Cycled Graphite Electrode in Lithium-Ion Cells. *J. Power Sources* **2011**, *196* (20), 8719–8727. https://doi.org/10.1016/j.jpowsour.2011.05.079.

(10) Moshiel Biton; Vladimir Yufit; Farid Tariq, a M. K. and N. B. Enhanced Imaging of Lithium Ion Battery Electrode Materials. *J. Electrochem. Soc.* **2017**, *164* (1), A6032–A6038. https://doi.org/10.1149/2.0061701jes.

(11) Martha, S. K.; Nanda, J.; Kim, Y.; Unocic, R. R.; Pannala, S.; Dudney, N. J. Solid Electrolyte Coated High Voltage Layered-Layered Lithium-Rich Composite Cathode: Li 1.2 Mn 0.525 Ni 0.175 Co 0.1 O 2 †. *J. Mater. Chem. A* **2013**, *1*, 5587–5595. https://doi.org/10.1039/c3ta10586e.

(12) Scipioni, R.; Jørgensen, P. S.; Stroe, D. I.; Younesi, R.; Simonsen, S. B.; Norby, P.; Hjelm, J.; Jensen, S. H. Complementary Analyses of Aging in a Commercial LiFePO4/Graphite 26650 Cell. *Electrochim. Acta* **2018**, *284*, 454–468. https://doi.org/10.1016/j.electacta.2018.07.124.

(13) Deng, Z.; Lin, X.; Huang, Z.; Meng, J.; Zhong, Y.; Ma, G.; Zhou, Y.; Shen, Y.; Ding, H.; Huang, Y. Recent Progress on Advanced Imaging Techniques for Lithium-Ion Batteries. *Adv. Energy Mater.* **2021**, *11* (2), 2000806. https://doi.org/10.1002/AENM.202000806.

(14) Xiao, C.; Li, Z.; Guthrey, H.; Moseley, J.; Yang, Y.; Wozny, S.; Moutinho, H.; To, B.; Berry, J. J.; Gorman, B.; Yan, Y.; Zhu, K.; Al-Jassim, M. Mechanisms of Electron-Beam-Induced Damage in Perovskite Thin Films Revealed by Cathodoluminescence Spectroscopy. *J. Phys. Chem. C* **2015**, *119* (48), 26904–26911. https://doi.org/10.1021/ACS.JPCC.5B09698/ASSET/IMAGES/LARGE/JP-2015-09698X_0007.JPEG.

(15) Hutzenlaub, T.; Thiele, S.; Paust, N.; Spotnitz, R.; Zengerle, R.; Walchshofer, C. Three-Dimensional Electrochemical Li-Ion Battery Modelling Featuring a Focused Ion-Beam/Scanning Electron Microscopy Based Three-Phase Reconstruction of a LiCoO2 Cathode. *Electrochim. Acta* **2014**, *21*, 131–139. https://doi.org/10.1016/j.electacta.2013.10.103.

(16) Park, K.-J.; Hwang, J.-Y.; Ryu, H.-H.; Maglia, F.; Kim, S.-J.; Lamp, P.; Yoon, C. S.; Sun, Y.-K. Degradation Mechanism of Ni-Enriched NCA Cathode for Lithium Batteries: Are Microcracks Really Critical? *ACS Energy Lett* **2021**, *15*, 36. https://doi.org/10.1021/acsenergylett.9b00733.

(17) Li, J.; Manthiram, A. A Comprehensive Analysis of the Interphasial and Structural Evolution over Long-Term Cycling of Ultrahigh-Nickel Cathodes in Lithium-Ion Batteries. *Adv. Energy Mater.* **2019**, *9* (45), 1902731. https://doi.org/10.1002/aenm.201902731.

(18) Rosser, T. E.; Dickinson, E. J. F.; Raccichini, R.; Hunter, K.; Searle, A. D.; Kavanagh, C. M.; Curran, P. J.; Hinds, G.; Park, J.; Wain, A. J. Improved Operando Raman Cell Configuration for Commercially-Sourced Electrodes in Alkali-Ion Batteries. *J. Electrochem. Soc.* **2021**, *168* (7), 070541. https://doi.org/10.1149/1945-7111/AC132D.

(19) Cho, S. J.; Chung, C. C.; Podowitz-Thomas, S.; Jones, J. L. Understanding the Lithium Deficient Li x Ni y Mn z Co 1-y-z O 2 (X < 1) Cathode Materials Structure. *Mater. Chem. Phys.* **2019**, *228*, 32–36. https://doi.org/10.1016/j.matchemphys.2019.02.028.

(20) Nanda, J.; Remillard, J.; O'Neill, A.; Bernardi, D.; Ro, T.; Nietering, K. E.; Go, J. Y.; Miller, T. J. Local State-of-Charge Mapping of Lithium-Ion Battery Electrodes. *Adv. Funct. Mater.* **2011**, *21* (17), 3282–3290. https://doi.org/10.1002/adfm.201100157.

(21) Sole, C.; Drewett, N. E.; Hardwick, L. J. Insitu Raman Study of Lithium-Ion Intercalation into Microcrystalline Graphite. *Faraday Discuss.* **2014**, *172*, 223–237. https://doi.org/10.1039/c4fd00079j.

(22) Li, G.; Li, H.; Mo, Y.; Chen, L.; Huang, X. Further Identification to the SEI Film on Ag Electrode in Lithium Batteries by Surface Enhanced Raman Scattering (SERS). *J. Power Sources* **2002**, *104* (2), 190–194. https://doi.org/10.1016/S0378-7753(01)00908-9.

(23) Cowan, A. J.; Hardwick, L. J. Advanced Spectroelectrochemical Techniques to Study Electrode Interfaces Within Lithium-Ion and Lithium-Oxygen Batteries. *Annu. Rev. Anal. Chem.* **2019**, *12*, 323–346. https://doi.org/10.1146/ANNUREV-ANCHEM-061318-115303.

(24) Wu, Q.; Maroni, V. A.; Gosztola, D. J.; Miller, D. J.; Dees, D. W.; Lu, W. A Raman-Based Investigation of the Fate of Li 2 MnO 3 in Lithium- and Manganese-Rich Cathode Materials for Lithium Ion Batteries . *J. Electrochem. Soc.* **2015**, *162* (7), A1255–A1264.

https://doi.org/10.1149/2.0631507jes.

(25) Sethuraman, V. A.; Hardwick, L. J.; Srinivasan, V.; Kostecki, R. Surface Structural Disordering in Graphite upon Lithium Intercalation/Deintercalation. *J. Power Sources* **2010**, *195* (11), 3655–3660. https://doi.org/10.1016/j.jpowsour.2009.12.034.

(26) Pollard, A. J.; Brennan, B.; Stec, H.; Tyler, B. J.; Seah, M. P.; Gilmore, I. S.; Roy, D. Quantitative Characterization of Defect Size in Graphene Using Raman Spectroscopy. *Appl. Phys. Lett.* **2014**, *105* (25), 253107. https://doi.org/10.1063/1.4905128.

(27) Julien, C. M.; Mauger, A. In Situ Raman Analyses of Electrode Materials for Li-Ion Batter. *AIMS Mater. Sci.* **2018**, *5* (4), 650–698. https://doi.org/10.3934/matersci.2018.4.650.

(28) Baddour-Hadjean, R.; Pereira-Ramos, J. P. Raman Microspectrometry Applied to the Study of Electrode Materials for Lithium Batteries. *Chem. Rev.* **2010**, *110* (3), 1278–1319. https://doi.org/10.1021/cr800344k.

(29) Ruther, R. E.; Callender, A. F.; Zhou, H.; Martha, S. K.; Nanda, J. Raman Microscopy of Lithium-Manganese-Rich Transition Metal Oxide Cathodes. *J. Electrochem. Soc.* **2015**, *162* (1), A98–A102. https://doi.org/10.1149/2.0361501jes.

(30) Zhang, X.; Mauger, A.; Lu, Q.; Groult, H.; Perrigaud, L.; Gendron, F.; Julien, C. M. Synthesis and Characterization of LiNi1/3Mn1/3Co1/3O2 by Wet-Chemical Method. *Electrochim. Acta* **2010**, *55* (22), 6440–6449. https://doi.org/10.1016/J.ELECTACTA.2010.06.040.

(31) Flores, E.; Novák, P.; Aschauer, U.; Berg, E. J. Cation Ordering and Redox Chemistry of Layered Ni-Rich Li XNi1-2 YCo YMn YO2: An Operando Raman Spectroscopy Study. *Chem. Mater.* **2020**, *32* (1), 186–194. https://doi.org/10.1021/acs.chemmater.9b03202.

(32) Sharma, N.; Montserrat, G.; Mestres, S.; Liqiang, M.; Berg, E. J.; Flores, E.; Novák, P. In Situ and Operando Raman Spectroscopy of Layered Transition Metal Oxides for Li-Ion Battery Cathodes. *Front. Energy Res.* **2018**, *1*, 82. https://doi.org/10.3389/fenrg.2018.00082.

(33) Li, C. Y.; Tian, Z. Q.; Yu, Y.; Wang, C.; Zhang, Y.; Zheng, S. Y.; Li, J. F.; Maglia, F.; Jung, R.;

Shao-Horn, Y. Surface Changes of LiNixMnyCo1-x-YO2 in Li-Ion Batteries Using in Situ Surface-Enhanced Raman Spectroscopy. *J. Phys. Chem. C* **2020**, *124* (7), 4024–4031. https://doi.org/10.1021/acs.jpcc.9b11677.

(34) Fang, S.; Yan, M.; Hamers, R. J. Cell Design and Image Analysis for in Situ Raman Mapping of Inhomogeneous State-of-Charge Profiles in Lithium-Ion Batteries. *J. Power Sources* **2017**, *352*, 18–25. https://doi.org/10.1016/j.jpowsour.2017.03.055.

(35) Weatherup, R. Observing Degradation at Electrode-Electrolyte Interfaces in Li-Ion Batteries. In *Proc. SPIE 11883, Photoemission Spectroscopy for Materials Analysis*; SPIE, 2021; Vol. 11883, p 1188306. https://doi.org/10.1117/12.2604797.

(36) Lee, J. T.; Nitta, N.; Benson, J.; Magasinski, A.; Fuller, T. F.; Yushin, G. Comparative Study of the Solid Electrolyte Interphase on Graphite in Full Li-Ion Battery Cells Using X-Ray Photoelectron Spectroscopy, Secondary Ion Mass Spectrometry, and Electron Microscopy. *Carbon N. Y.* **2013**, *52*, 388–397. https://doi.org/10.1016/j.carbon.2012.09.049.

(37) An, S. J.; Li, J.; Daniel, C.; Mohanty, D.; Nagpure, S.; Wood, D. L. The State of Understanding of the Lithium-Ion-Battery Graphite Solid Electrolyte Interphase (SEI) and Its Relationship to Formation Cycling. *Carbon N. Y.* **2016**, *105*, 52–76. https://doi.org/10.1016/j.carbon.2016.04.008.

(38) Edström, K.; Herstedt, M.; Abraham, D. P. A New Look at the Solid Electrolyte Interphase on Graphite Anodes in Li-Ion Batteries. *J. Power Sources* **2006**, *153* (2), 380–384. https://doi.org/10.1016/j.jpowsour.2005.05.062.

(39) Fu, Z.; Hu, J.; Hu, W.; Yang, S.; Luo, Y. Quantitative Analysis of Ni 2+ /Ni 3+ in Li[Ni x Mn y Co z]O 2 Cathode Materials: Non-Linear Least-Squares Fitting of XPS Spectra. *Appl. Surf. Sci.* **2018**, *441*, 1048–1056. https://doi.org/10.1016/j.apsusc.2018.02.114.

(40) Andersson, A. M.; Henningson, A.; Siegbahn, H.; Jansson, U.; Edström, K. Electrochemically Lithiated Graphite Characterised by Photoelectron Spectroscopy. *J. Power Sources* **2003**, *119*–

121, 522–527. https://doi.org/10.1016/S0378-7753(03)00277-5.

(41) Major, G. H.; Avval, T. G.; Moeini, B. Assessment of the Frequency and Nature of Erroneous X-Ray Photoelectron Spectroscopy Analyses in the Scientific Literature. *J. Vac. Sci. Technol. A* **2020**, *38*, 61204. https://doi.org/10.1116/6.0000685.

(42) Wood, K. N.; Teeter, G. XPS on Li-Battery-Related Compounds: Analysis of Inorganic SEI Phases and a Methodology for Charge Correction. *ACS Appl. Energy Mater.* **2018**, *1* (9), 4493–4504. https://doi.org/10.1021/acsaem.8b00406.

(43) Otto, S. K.; Moryson, Y.; Krauskopf, T.; Peppler, K.; Sann, J.; Janek, J.; Henss, A. In-Depth Characterization of Lithium-Metal Surfaces with XPS and ToF-SIMS: Toward Better Understanding of the Passivation Layer. *Chem. Mater.* **2021**, *33* (3), 859–867. https://doi.org/10.1021/acs.chemmater.0c03518.

(44) Oswald, S.; Hoffmann, M.; Zier, M. Peak Position Differences Observed during XPS Sputter Depth Profiling of the SEI on Lithiated and Delithiated Carbon-Based Anode Material for Li-Ion Batteries. *Appl. Surf. Sci.* **2017**, *401*, 408–413. https://doi.org/10.1016/j.apsusc.2016.12.223.

(45) Ciosek Högström, K.; Malmgren, S.; Hahlin, M.; Gorgoi, M.; Nyholm, L.; Rensmo, H.; Edström, K. The Buried Carbon/Solid Electrolyte Interphase in Li-Ion Batteries Studied by Hard x-Ray Photoelectron Spectroscopy. *Electrochim. Acta* **2014**, *138*, 430–436. https://doi.org/10.1016/j.electacta.2014.06.129.

(46) Brundle, C. R.; Crist, B. V.; Bagus, P. S. Accuracy Limitations for Composition Analysis by XPS Using Relative Peak Intensities: LiF as an Example. *J. Vac. Sci. Technol. A Vacuum, Surfaces, Film.* **2020**, *39* (1), 013202. https://doi.org/10.1116/6.0000674.

(47) Li, D.; Li, H.; Danilov, D. L.; Gao, L.; Chen, X.; Zhang, Z.; Zhou, J.; Eichel, R. A.; Yang, Y.; Notten, P. H. L. Degradation Mechanisms of C6/LiNi0.5Mn0.3Co0.2O2 Li-Ion Batteries Unraveled by Non-Destructive and Post-Mortem Methods. *J. Power Sources* **2019**, *416*, 163–174. https://doi.org/10.1016/J.JPOWSOUR.2019.01.083.

(48) Martha, S. K.; Sclar, H.; Szmuk Framowitz, Z.; Kovacheva, D.; Saliyski, N.; Gofer, Y.; Sharon, P.; Golik, E.; Markovsky, B.; Aurbach, D. A Comparative Study of Electrodes Comprising Nanometric and Submicron Particles of LiNi0.50Mn0.50O2, LiNi0.33Mn0.33Co0.33O2, and LiNi0.40Mn0.40Co0.20O2 Layered Compounds. *J. Power Sources* **2009**, *189* (1), 248–255. https://doi.org/10.1016/J.JPOWSOUR.2008.09.090.

(49) Liu, S.; Su, J.; Zhao, J.; Chen, X.; Zhang, C.; Huang, T.; Wu, J.; Yu, A. Unraveling the Capacity Fading Mechanisms of LiNi0.6Co0.2Mn0.2O2 at Elevated Temperatures. *J. Power Sources* **2018**, *393*, 92–98. https://doi.org/10.1016/J.JPOWSOUR.2018.05.029.

(50) Biesinger, M. C.; Payne, B. P.; Grosvenor, A. P.; Lau, L. W.; Gerson, A. R.; StC Smart, R. Resolving Surface Chemical States in XPS Analysis of First Row Transition Metals, Oxides and Hydroxides: Cr, Mn, Fe, Co and Ni. *Appl. Surf. Sci.* **2011**, *257*, 2717–2730. https://doi.org/10.1016/j.apsusc.2010.10.051.

(51) Harrison, K.; Hazell, L. B. The Determination of Uncertainties in Quantitative XPS/AES and Its Impact on Data Acquisition Strategy. *Surf. Interface Anal.* **1992**, *18* (5), 368–376. https://doi.org/10.1002/SIA.740180510.

(52) Pieczonka, N. P. W.; Liu, Z.; Lu, P.; Olson, K. L.; Moote, J.; Powell, B. R.; Kim, J. Understanding Transition-Metal Dissolution Behavior in LiNi0.5Mn1.5O4 High-Voltage Spinel for Lithium Ion Batteries. *J. Phys. Chem. C* **2013**, *117* (31), 15947–15957. https://doi.org/https://doi.org/10.1021/jp405158m.

(53) Ruff, Z.; Xu, C.; Grey, C. P. Transition Metal Dissolution and Degradation in NMC811-Graphite Electrochemical Cells. *J. Electrochem. Soc.* **2021**, *168* (6), 060518. https://doi.org/10.1149/1945-7111/AC0359.

(54) Shard, A. G. Detection Limits in XPS for More than 6000 Binary Systems Using Al and Mg Kα X-Rays. *Surf. Interface Anal.* **2014**, *46* (3), 175–185. https://doi.org/10.1002/sia.5406.

(55) Shard, A. G. Practical Guides for X-Ray Photoelectron Spectroscopy: Quantitative XPS. *J. Vac.*

Sci. Technol. A **2020**, *38* (4), 041201. https://doi.org/10.1116/1.5141395.

(56) Magee, C. W.; Harrington, W. L. Depth Profiling of Sodium in SiO2 Films by Secondary Ion Mass Spectrometry. *Appl. Phys. Lett.* **1978**, *33* (2), 193–196. https://doi.org/10.1063/1.90271.

(57) Roberts, A.; Counsell, J. D. P.; Blomfield, C.; Pearse, A. *Argon Ion Gas Cluster Depth Profiling of Li Ion Thin-Film Battery Materials*; 2017. https://doi.org/10.13140/RG.2.2.32535.88480.

(58) Bondarchuk, O.; LaGrow, A. P.; Kvasha, A.; Thieu, T.; Ayerbe, E.; Urdampilleta, I. On the X-Ray Photoelectron Spectroscopy Analysis of LiNixMnyCozO2 Material and Electrodes. *Appl. Surf. Sci.* **2021**, *535*, 147699. https://doi.org/10.1016/J.APSUSC.2020.147699.

(59) Workman, M. J.; Beau, J.; Webber, W.; Perry, M. L.; Kalha, C.; Fernando, N. K.; Bhatt, P.; Johansson, F. O. L.; Lindblad, A.; Rensmo, H.; On, L.; Medina, Z.; Lindblad, R.; Siol, S.; Jeurgens, L. P. H.; Cancellieri, C.; Rossnagel, K.; Medjanik, K.; Schönhense, G.; Simon, M.; Gray, A. X.; Nemšák, S.; Lömker, P.; Schlueter, C.; Regoutz, A. Hard X-Ray Photoelectron Spectroscopy: A Snapshot of the State-of-the-Art in 2020. *J. Phys. Condens. Matter* **2021**, *33* (44pp), 233001. https://doi.org/10.1088/1361-648X/abeacd.

(60) Spencer, B. F.; Maniyarasu, S.; Reed, B. P.; Cant, D. J. H.; Ahumada-Lazo, R.; Thomas, A. G.; Muryn, C. A.; Maschek, M.; Eriksson, S. K.; Wiell, T.; Lee, T.-L.; Tougaard, S.; Shard, A. G.; Flavell, W. R. Inelastic Background Modelling Applied to Hard X-Ray Photoelectron Spectroscopy of Deeply Buried Layers: A Comparison of Synchrotron and Lab-Based (9.25 KeV) Measurements. *Appl. Surf. Sci.* **2021**, *541*, 148635. https://doi.org/10.1016/j.apsusc.2020.148635.

(61) Gibson, J. S.; Narayanan, S.; Swallow, J. E. N.; Kumar-Thakur, P.; Pasta, M.; Lee, T.-L.; Weatherup, R. S. Gently Does It!: In Situ Preparation of Alkali Metal–Solid Electrolyte Interfaces for Photoelectron Spectroscopy. *Faraday Discuss.* **2022**. https://doi.org/10.1039/D1FD00118C.

(62) Yamagishi, Y.; Morita, H.; Nomura, Y.; Igaki, E. Visualizing Lithium Distribution and

Degradation of Composite Electrodes in Sulfide-Based All-Solid-State Batteries Using Operando Time-of-Flight Secondary Ion Mass Spectrometry. *ACS Appl. Mater. Interfaces* **2021**, *13* (1), 580–586. https://doi.org/10.1021/acsami.0c18505.

(63) Peled, E.; Bar Tow, D.; Merson, A.; Gladkich, A.; Burstein, L.; Golodnitsky, D. Composition, Depth Profiles and Lateral Distribution of Materials in the SEI Built on HOPG-TOF SIMS and XPS Studies. *J. Power Sources* **2001**, *97–98*, 52–57. https://doi.org/10.1016/S0378-7753(01)00505-5.

(64) Gauthier, N.; Courrèges, C.; Demeaux, J.; Tessier, C.; Martinez, H. Probing the In-Depth Distribution of Organic/Inorganic Molecular Species within the SEI of LTO/NMC and LTO/LMO Batteries: A Complementary ToF-SIMS and XPS Study. *Appl. Surf. Sci.* **2020**, *501* (September 2019), 144266. https://doi.org/10.1016/j.apsusc.2019.144266.

(65) Seah, M. P.; Shard, A. G. The Matrix Effect in Secondary Ion Mass Spectrometry. *Appl. Surf. Sci.* **2018**, *439*, 605–611. https://doi.org/10.1016/J.APSUSC.2018.01.065.

(66) Lee, J. L. S.; Gilmore, I. S.; Seah, M. P.; Fletcher, I. W. Topography and Field Effects in Secondary Ion Mass Spectrometry – Part I: Conducting Samples. *J. Am. Soc. Mass Spectrom.* **2011**, *22* (10), s13361-011-0201–1. https://doi.org/10.1007/S13361-011-0201-1..

(67) Bessette, S.; Paolella, A.; Kim, C.; Zhu, W.; Hovington, P.; Gauvin, R.; Zaghib, K. Nanoscale Lithium Quantification in Li X Ni y Co w Mn Z O 2 as Cathode for Rechargeable Batteries OPEN. *Sci. RePORtS* | **2018**, *8*, 17575. https://doi.org/10.1038/s41598-018-33608-3.

(68) Li, W.; Dolocan, A.; Oh, P.; Celio, H.; Park, S.; Cho, J.; Manthiram, A. Dynamic Behaviour of Interphases and Its Implication on High-Energy-Density Cathode Materials in Lithium-Ion Batteries. *Nat. Commun.* **2017**, *8*. https://doi.org/10.1038/ncomms14589.

(69) Téllez, H.; Aguadero, A.; Druce, J.; Burriel, M.; Fearn, S.; Ishihara, T.; McPhail, D. S.; Kilner, J. A. New Perspectives in the Surface Analysis of Energy Materials by Combined Time-of-Flight Secondary Ion Mass Spectrometry (ToF-SIMS) and High Sensitivity Low-Energy Ion

Scattering (HS-LEIS). *J. Anal. At. Spectrom.* **2014**, *29* (8), 1361–1370. https://doi.org/10.1039/c3ja50292a.

(70) Yamagishi, Y.; Morita, H.; Nomura, Y.; Igaki, E. Visualizing Lithiation of Graphite Composite Anodes in All-Solid-State Batteries Using *Operando* Time-of-Flight Secondary Ion Mass Spectrometry. *J. Phys. Chem. Lett.* **2021**, *12* (19), 4623–4627. https://doi.org/10.1021/acs.jpclett.1c01089.

For Table of Contents Only